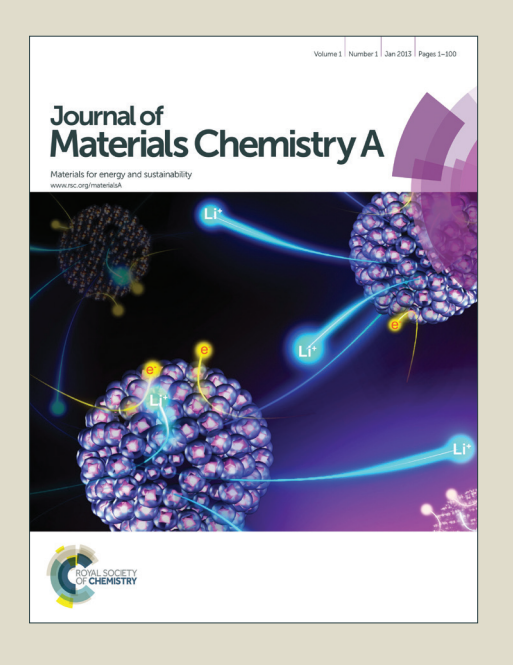
Journal of Materials Chemistry A

Accepted Manuscript



This is an *Accepted Manuscript*, which has been through the Royal Society of Chemistry peer review process and has been accepted for publication.

Accepted Manuscripts are published online shortly after acceptance, before technical editing, formatting and proof reading. Using this free service, authors can make their results available to the community, in citable form, before we publish the edited article. We will replace this Accepted Manuscript with the edited and formatted Advance Article as soon as it is available.

You can find more information about *Accepted Manuscripts* in the **Information for Authors**.

Please note that technical editing may introduce minor changes to the text and/or graphics, which may alter content. The journal's standard <u>Terms & Conditions</u> and the <u>Ethical guidelines</u> still apply. In no event shall the Royal Society of Chemistry be held responsible for any errors or omissions in this *Accepted Manuscript* or any consequences arising from the use of any information it contains



$\label{eq:continuous} Ultrafast\ Nano-Spherical\ Single-Crystalline\ of\ LiMn_{0.792}Fe_{0.198}Mg_{0.010}PO_4$ $Solid-Solution\ Confined\ among\ Unbundled\ Interstices\ of\ SGCNT$

Kazuaki Kisu¹, Etsuro Iwama^{1,3}, Wataru Onishi¹, Shota Nakashima¹, Wako Naoi², and Katsuhiko Naoi*^{1,2,3}

¹Department of Applied Chemistry, Tokyo University of Agriculture & Technology, 2-24-16 Naka-cho, Koganei, Tokyo 184-8558, Japan

^{*}E-mail: <u>k-naoi@cc.tuat.ac.jp</u>

²Division of Arts and Sciences, K & W Inc., 1-3-16-901 Higashi, Kunitachi, Tokyo 186-0002, Japan

³Advanced Capacitor Research Center, Tokyo University of Agriculture & Technology, 2-24-16 Naka-cho, Koganei, Tokyo 184-8558, Japan

Abstract

Spherical LiMn_{0.792}Fe_{0.198}Mg_{0.010}PO₄ nanocrystals, which are highly dispersed and encapsulated within the interstices of supergrowth (single-walled) carbon nanotubes (SGCNTs), were successfully synthesized by *in situ* material processing technology called "ultra centrifuging (UC) treatment". TEM images of these LiMn_{0.792}Fe_{0.198}Mg_{0.010}PO₄/SGCNT composites suggest the direct attachment of the LiMn_{0.792}Fe_{0.198}Mg_{0.010}PO₄ nanocrystals (10-40 nm) onto the surface of highly conductive SGCNT. The Mg-doping brought out 10% increase of Li⁺ capacity in Mn site with 200% increase of Li⁺ diffusivity and 50 % decrease of electric resistance owing to such peculiar "nano-nano LiMn_{0.792}Fe_{0.198}Mg_{0.010}PO₄/SGCNT composites". The synthesized LiMn_{0.792}Fe_{0.198}Mg_{0.010}PO₄/SGCNT composites overcome the inherent restrictions of one-dimensional diffusion and deliver high electrochemical capacity density of *ca*. 54 mA h g⁻¹ per composite (corresponding to 77 mA h g⁻¹ per pure LiMn_{0.792}Fe_{0.198}Mg_{0.010}PO₄) at a high rate of 50 C, while showing excellent cycle life, retaining 84% of the initial capacity over 3,000 cycles.

Introduction

Orthorhombic phospho-olivine LiMPO₄ (M = Fe, 1 Mn, 2 Co, 3 and Ni⁴) compounds show impressive thermal and electrochemical stability, making them promising cathode materials for use in safer lithium-ion batteries (LIBs), especially with regard to automobile applications. Among phospho-olivine structure materials, LiFePO₄ in particular has been extensively studied as the potential cathode on the basis of its numerous appealing features giving its low cost and safety. However, its lithium storage performances are limited by its poor rate capability, making them promising cathode materials for use in safety at high charge-discharge features giving its low cost and safety. However, its lithium storage performances are limited by its poor rate capability, making them promising cathode materials for use in safety at high charge-discharge features giving its low cost and safety. However, its lithium storage performances are limited by its poor rate capability, making them promising cathode materials for use in safety at high charge-discharge giving its low cost and safety. However, its lithium storage performances are limited by its poor rate capability, making them promising cathode materials for use in safety at high charge-discharge giving its low cost and safety. However, its lithium storage performances are limited by its poor rate capability, and safety at high charge-discharge rate. The limitation results from the intrinsically low electrical conductivity (LiFePO₄: $10^{-9} - 10^{-10} \Omega^{-1}$ cm⁻¹) and slow diffusion of Li⁺ (LiFePO₄: $10^{-14} - 10^{-15}$ cm² s⁻¹) through its one-dimensional structural channels.

Numerous efforts have been made to address this problem. For example, tailoring the particle size into the nano-range shortens the ionic and electrical path length, ¹⁰ thereby improving electrochemical performances. Coating with conductive or using composites, such as carbon-based materials also improves performances by enhancing electrical conductivity. ^{11,12} The utility of these approaches is most apparent in the recent commercialization of LiFePO₄/carbon composites for power tool applications by the US venture company A123 Inc. ¹³ However, the low operating potential of LiFePO₄ (3.4 V vs. Li/Li⁺) restricts energy density,

which in turn limits its ability to be used in high power electrochemical energy storages (EES) in electric vehicles, their hybrids, and plug-in variants.¹⁴

Replacing the Fe atom with other transition metals, especially Mn, Co, or Ni can result in a higher energy density and allow for operation at higher potential. Out of these three possible alternatives, LiMnPO₄ is the most useful given that it possesses a mild operating potential (4.1 V vs. Li/Li⁺), and an identical capacity of LiFePO₄ (170 mA h g⁻¹), while LiCoPO₄ and LiNiPO₄ have much higher potentials (> 4.9 V vs. Li/Li⁺), but are problematic given tendency to oxidize most electrolytes on their electrode-electrolyte interface. Unfortunately, LiMnPO₄ suffers from even lower electrical $(10^{-14} - 10^{-15} \,\Omega^{-1} \, \text{cm}^{-1})^{15}$ conductivity and ionic $(10^{-14} - 10^{-17} \, \text{cm}^2 \, \text{s}^{-1})^{16}$ conductivities due to the Jahn-Teller lattice deformation and structural changes that occur during its cycling, ¹⁷ which result in much lower specific capacity, cycle stability, and rate capability. ^{18,19}

To overcome these limitations, multi-component systems have been developped. For example, Yamada and colleagues elucidated the LiMn_xFe_{1-x}PO₄ phase diagram, and showed that it forms a solid solution for all transition metal ratios. The electrochemical performance of such systems has also been studied, with tests showing that 20% dosage of Fe yields their best possible performance in terms of energy density and reversibility. Despite the improved electrochemical properties and the relative ease of available synthetic routes such as solid-state, and hydrothermal methods, the reported electrochemical performances of LiMn_xFe_{1-x}PO₄ is still not sufficient for practical applications. Several methods exist to resolve these issues; i) development of carbon composite materials or carbon coating, till tailoring particles size to reduce the Li⁺ path length, iii) cation doping into the LiMn_xFe_{1-x}PO₄ to increase both Li⁺ conductivity and electric conductivity.

For example, Yoshida and coworkers recently reported improved electrochemical performance for LiMnPO₄ using a hydrothermal method to synthesize particles of about 40 nm in size.³⁰ Electrochemical characterization showed an excellent rate capability deliviering 120 mA h g⁻¹ at 10C, while their EELS mapping indicates that the observed improvement in properties resulted from the shortened Li⁺ diffusion path. In addition to changing particle size, improved performances on the capacity delivery, cycle life, and rate capability of LiMn_xFe_{1-x}PO₄ can be achieved by a cation doping of such Ni,³¹ Co,³² Zn,³³ Mg,^{20,34} Gd,³⁵ V,³⁵ Cu,³⁶ Ti,³⁷ Zr,³⁷ Sn,³⁸ Al,²⁹ and W.²⁹ Divalent cation substitution using Mg²⁺, Zn²⁺ Cu²⁺, Ni²⁺, or Co²⁺ was shown to significantly improve conductivity as well. Doping of Mg²⁺ in particular decreases the lattice misfits near the LiFe_{0.48}Mn_{0.48}Mg_{0.04}PO₄ / Fe_{0.48}Mn_{0.48}Mg_{0.04}PO₄ boundary due to the formation

of pseudo-one phase reaction during Li⁺ extraction.³⁹ However, although minimizing particle size and taking advantage of cation doping has allowed for high rate performance up to 20C, the high performance over 50C was yet to be achieved. Recently, Wang *et al.* reported the LiMn_{0.75}Fe_{0.25}PO₄ nanorods grown on graphene sheets, which delivers 65 mA h g⁻¹ per LiMn_{0.75}Fe_{0.25}PO₄ at 100C and even 40 mA h g⁻¹ at 150C with the discharge cut-off voltage of 2.0 V.⁴⁰ Their results also suggest that the direct coating of LiMn_{0.75}Fe_{0.25}PO₄ nanorods on the graphene surface delivers far superior electrochemical performance compared to the physical mixture of the two materials.

Herein, we have synthesized nanoscale $LiMn_{0.792}Fe_{0.198}Mg_{0.010}PO_4$ particles build-up and simultaneously composited with supergrowth (single-walled) carbon nanotubes $(SGCNT)^{41,42}$ in a one-step synthesis using an original method named ultra-centrifuging (UC) treatment. UC treatment is a build-up synthetic scheme involving i) unbundling of bunchy SGCNTs, ii) *in-situ* sol-gel reaction of $LiMn_{0.792}Fe_{0.198}Mg_{0.010}PO_4$ precursors on the exposed SGCNT surface, iii) restructuring of SGCNT matrix.

The subsequent short-duration heat treatment (post-UC treatment) effectively and simultaneously completed the crystallization of LiMn_{0.8}Fe_{0.2}PO₄ and Mg doping into the LiMn_{0.8}Fe_{0.2}PO₄ structure without crystal growth. Note that this work follows previous success in synthesizing nano-sized crystalline metal oxide/carbon composite materials, RuO₂/Ketjen Black (KB), ⁴³ Li₄Ti₅O₁₂/carbon nanofiber(CNF), ^{44,45} SnO₂/KB, ⁴⁶ and 0.7Li₂MnO₃-0.3LiCo_{0.3}Ni_{0.3}Mn_{0.3}O₂/CNF composites. ⁴⁷ In this study, we will present the desired nano-sized (10-40 nm) LiMn_{0.792}Fe_{0.198}Mg_{0.010}PO₄ particles hyper dispersed and encapsulated within the interstices of SGCNT, delivering a high rate electrochemical performance of *ca.* 54 mA h g⁻¹ per composite (corresponding to 77 mA h g⁻¹ per pure LiMn_{0.792}Fe_{0.198}Mg_{0.010}PO₄) at 50C. Detailed evaluation of the structural feature and electrochemical properties in the UC-synthesized LiMn_{0.792}Fe_{0.198}Mg_{0.010}PO₄/SGCNT were investigated with the aim of determining the optimum features necessary for the alternative high energy cathode material in high-power typed LIBs.

Experimental

[Materials]

LiNO₃ (\geq 98%), Mn(NO₃)₂·6H₂O (\geq 98%), Fe(NO₃)₃·9H₂O (\geq 98%), Mg(NO₃)₂·6H₂O (\geq 98%), H₃PO₄ (\geq 85%), and C₆H₈O₇ (\geq 98%) were all acquired from Wako Pure Chemical (Japan) and were used as Li, Mn, Fe, Mg, and PO₄ sources, and as a chelating agent, respectively.

Supergrowth (single-walled) carbon nanotube (SGCNT⁴¹; average D/G=0.40, see Fig. S1) received from ZEON Corp. was selected as a carbon matrix because of its high electronic conductivity, ⁴² heat conduction ranging broadly from 100-10,000 W m⁻¹ K⁻¹, ⁴⁸ and high specific surface area (900 m² g⁻¹). SGCNT was used without further purification.

(DMF) (Wako Pure Chemical, Japan; ≥98%) was used as solvents throughout.

$[LiMn_{0.792}Fe_{0.198}Mg_{0.010}PO_4/SGCNT synthesis]$

Two kinds of solution (solution A and B) were prepared. Solution A was composed of 0.132~g (1.00~eq.) of LiNO₃, 0.436~g (0.792~eq.) of Mn(NO₃)₂·6H₂O, 0.153~g (0.198~eq.) of Fe(NO₃)₃·9H₂O, 0.00492~g (0.010~eq.) of Mg(NO₃)₂·6H₂O, and 0.369~g (1.00~eq.) of C₆H₈O₇ dissolved in 15.0~g of DMF. Solution B was composed of 0.221~g (1.00~eq.) of H₃PO₄ dissolved in 5.00~g of DMF. Solution A, solution B, 8.00~g of DMF, and 0.129~g of SGCNT were subjected to UC treatment, whereby 75,000g of mechano-chemical agitation applied to the whole mixture for 5 min to give the blackish gel. After drying it at $80~^{\circ}$ C for 12~h~in~vacuo (ultimate vacuum = 0.67~eq Pa), the precursor LiMn_{0.792}Fe_{0.198}Mg_{0.010}PO₄/SGCNT composite was obtained. The precursor powder was then annealed for 8~min (heating : 3~min, holding : 5~min) at $700~^{\circ}$ C under nitrogen flow to give the nano-crystalline LiMn_{0.792}Fe_{0.198}Mg_{0.010}PO₄/SGCNT.

[Physicochemical characterizations]

LiMn_{0.792}Fe_{0.198}Mg_{0.010}PO₄/ SGCNT nanostructure and particle size distribution were characterized by high-resolution transmission electron microscopy (HRTEM, Japan, Hitachi model H9500, 300 kV), while the crystal structure was analyzed using X-ray diffraction (XRD, Rigaku SmartLab, Cu K α radiation λ = 1.54056 Å, operating at 45 kV - 200 mA). Thermogravimetric analysis (TGA) was used to confirm composite stoichiometry, and was performed under synthetic air using a thermogravimetric and differential thermal analyzer (Seiko Instruments TG/DTA6300).

[Electrochemical characterizations]

The electrochemical half-cell was based on a 2032 coin design and was assembled using Li metal and LiMn_{0.792}Fe_{0.198}Mg_{0.010}PO₄/SGCNT electrodes. The LiMn_{0.792}Fe_{0.198}Mg_{0.010}PO₄/SGCNT electrode was prepared by mixing the composite and polyvinylidene difluoride (PVdF) in a 90/10 mass ratio in N-methyl pyrrolidone (NMP). The mixture was coated on an Al foil (current collector) and dried at 80 °C *in vacuo* (ultimate

vacuum = 0.67 Pa) for 12 h. The electrode and its loading weight were designed to be *ca.* 20 μm thick, 0.4 mg cm⁻², respectively. The used electrolyte was a 1.0 M solution of lithium hexafluorophosphate (LiPF₆) dissolved in a mixture of ethylene carbonate (EC) and diethyl carbonate (DEC) in a 50/50 volume ratio. The used separator was 25 μm-thick polypropylene film (Cellgard2400). Charge-discharge tests were performed between 2.5 - 4.5 V *vs.* Li/Li⁺ under CC-CV mode at several current densities ranging from 0.1C to 50C rate assuming 1C-rate being 170 mA g⁻¹. Long-term cycling tests were conducted between 2.5 - 4.5 V *vs.* Li/Li⁺ under CC mode at a fixed charge-discharge rate of 1C.

Results and discussion

[Material Design and Synthetic Optimization]

Major compositions and crystallographic parameters (x, y and z) of the UC-synthesized resulting composites ($\text{LiMn}_x\text{Fe}_y\text{Mg}_z\text{PO}_4$ (x+y+z=1)/SGCNT) were characterized. Firstly, we checked the weight of SGCNT to the synthesized crystals ($\text{LiMn}_x\text{Fe}_y\text{Mg}_z\text{PO}_4$) with thermogravimetric analysis (TGA). Second, the atomic ratios for Mn:Fe (=x:y) as well as the Mg-doping (z) were verified by the Rietveld refinements of the XRD analysis.

As shown in Fig. 1 left (A) and (B), the obtained SGCNT ratios were 30% for the two typical samples of (A) LiMn_xFe_yPO₄/SGCNT and (B) LiMn_xFe_yMg_xPO₄ (z =0.01*)/SGCNT (*: the optimum ratio of z. This will be determined in the later section of XRD). Similar TGA curves within a error of 2% were obtained for other samples with various Mg doping levels z=0-0.05 as examined using our UC synthetic procedure (data not shown). This 30% amount is consistent with the initial dosage of SGCNT (30%), as shown in experimental sections, showing that our in-situ synthesis formed LiMn, Fe, Mg, PO₄/SGCNT composite stoichiometrically maintaining its ratio being 70/30 in mass even with a SGCNT presence during UC and/or post-UC process. namely, annealing. For the reference, pristine SGCNT has been exemplified under the same TGA conditions (shown in Fig. 1 left (C)). The curve shows a sudden decrease in its weight from 600°C, which is typical behavior of the carbon combustion under air. Interestingly, a large difference (170°C) was observed in the decomposition temperature of the SGCNT in its pristine (C) and their composite forms (A, B). Such temperature shifts are often observed in other reports of nano-scale metal oxides/carbon composites 44-47,49; to be more precise, 5-20 nm $\text{Li}_4\text{Ti}_5\text{O}_{12}$ (temperature shift=150°C), 44,45 2-4 nm SnO₂ (=170°C), 46 100 nm $0.7 \text{Li}_2 \text{MnO}_3 - 0.3 \text{LiCo}_{0.3} \text{Ni}_{0.3} \text{Mn}_{0.3} \text{O}_2^{47}$ (=180°C), and 5-10 nm anatase-TiO₂ ⁵⁰ (=100°C)

composited with various carbons like carbon blacks and nanotubes. In the case of the LiMn_xFe_yMg_zPO₄, 170°C lies within the range of reported temperature shifts ranging from 100-180°C. This may be partially explained by the catalytic influence of the co-existing LiMn_xFe_yMg_zPO₄ nanocrystals on SGCNT oxidative decomposition. Of course it depends very much on how those LiMn_xFe_yMg_zPO₄ crystals are accommodated with SGCNT: for instance, on the surface phases, inner tubes, edges on the disorder, or on the basal. We will address those issues further when the HRTEM is discussed.

The representative XRD patterns of LiMn_xFe_yMg_zPO₄/SGCNT (70/30) are shown in Fig. 1 right for the same samples. The ratio of Mn/Fe (=x/y) in the synthesized LiMn_yFe_yMg_zPO₄/SGCNT (70/30) was determined as 4, as indicated by the calculated refined lattice (a, b, and c-parameters) for the sample of (A) and (B) shown in Table 1. Those values are in consistent with the reported value of LiMn_{0.8}Fe_{0.2}PO₄ ⁵¹ (shown as (C) in Table 1). The proportional decrease of a, b, and c-lattice parameters for LiM_{0.8(1-z)}Fe_{0.2(1-z)}Mg_zPO₄ with an increase of Mg dosage ratio suggest the successful Mg doping into the LiMn_{0.8}Fe_{0.2}PO₄ structure (see Fig. S2). Furthermore, the optimum content of Mg (z) in the LiMn_xFe_yMg_zPO₄ crystal has been determined as z=0.01 through our preliminary experiments varying z=0.01-0.05 for their crystallographic nature and electrochemistry especially focused on the reversibility and rate-capability. The obtained Mg-doped crystals characterized generally as $LiMn_{0.8(1-z)}Fe_{0.2(1-z)}Mg_zPO_4$ (z=0.01-0.05) show essentially no differences in all of the peak patterns as indicated in a representative data for LiMn_{0.792}Fe_{0.198}Mg_{0.010}PO₄ (z=0.01) (see Fig. 1 right (B)). Theoretically speaking, increasing z-value brings about the decrease in the reversible capacity by 5% with z=0.05. High z value may also cause any possible cation mixing between Li and Mg in the crystal structure, which would in turn inhibit smooth one-dimensional Li diffusion along the b-axis of LiMn_{0.8(1-z)}Fe_{0.2(1-z)}Mg_zPO₄. Therefore, it should be unsurprising that the best electrochemical performance was obtained with z=0.01; this sample delivered both high reversible capacity of ca. 112 mA h g⁻¹ per composite at 0.1C and high rate capability of ca. 54 mA h g⁻¹ per composite at 50C.

[Structural Control to Nano-sized Solid-solution]

The nanostructure and crystallinity of the LiMn_{0.792}Fe_{0.198}Mg_{0.010}PO₄/SGCNT was observed by HRTEM (see Fig. 2). Fig. 2a shows that most of the LiMn_{0.792}Fe_{0.198}Mg_{0.010}PO₄ particles are spherical, uniformly dispersed and entangled within the SGCNT network, and range in size from 10 to 40 nm. On the other hand, the SGCNT is unusually well unbundled and stabilized

with an incorporation of the number of LiMn_{0.792}Fe_{0.198}Mg_{0.010}PO₄ particles in the whole entity of the composites. Such degree of unbundling specifically for the case of single-walled CNT is oftentimes very difficult using other chemical (surfactants⁵²) and mechanical protocols (jet-milling⁵³) attempted so far in previous papers. Our UC treatment, as a matter of fact, reveals to provide one of the best ways to proceed a non-equilibrium unbundling followed by an instantaneous confinements of the precursors of the crystals that will be cured by annealing process; then entangled and integrated within interstitial network of SGCNT forests as illustrated in Fig. 2b. Such entanglement and high-dispersion of the LiMn_{0.792}Fe_{0.198}Mg_{0.010}PO₄ particles within the SGCNTs' interstices establishes the lithium ion path and electron path, resulting in the excellent electrochemical properties, which will be discussed in the later section (Fig. 3).

The higher HRTEM image focused on a one LiMn_{0.792}Fe_{0.198}Mg_{0.010}PO₄ particle, as shown in Fig. 2c, reveals a complete solid solution of LiMn_{0.792}PO₄ and LiFe_{0.198}PO₄ in atomic ratio of Mn: Fe = 0.792: 0.198. Yet, 1% of Mg atoms are supposed to be substituted with Mn and Fe in the same proportions. The image also shows a single LiMn_{0.792}Fe_{0.198}Mg_{0.010}PO₄ crystal with the lattice of (101-plane; d-spacing of 4.31Å). No apparent mismatched and disordered crystal lattice was observed with and without Mg doping (see Fig. S3), suggesting the successful preparation of solid solution of LiMn_{0.792}Fe_{0.198}Mg_{0.010}PO₄. The electron diffraction (ED) patterns show clear spots corresponding to (301), (112), and (311) planes of LiMnPO₄ groups, and rings corresponding to (101) and (002) of SGCNTs (Fig. S4). These ED patterns confirm the existence of highly crystalline LiMn_{0.792}Fe_{0.198}Mg_{0.010}PO₄ in the presence of SGCNT, which is in good agreement with the XRD measurements (Fig. 1 right). The schematic illustration of the corresponding LiMn_{0.792}Fe_{0.198}Mg_{0.010}PO₄ crystal (Fig. 2c) is shown in Fig. 2d. Due to its single crystallinity and spherical morphology, the LiMn_{0.792}Fe_{0.198}Mg_{0.010}PO₄ crystal possesses a straight 1-D diffusion toward *b* direction with the path length shorter than 40 nm.

[Electrochemical Performances]

Charge-discharge tests were performed on both LiMn_{0.8}Fe_{0.2}PO₄ /SGCNT and LiMn_{0.792}Fe_{0.198}Mg_{0.010}PO₄/SGCNT to investigate the effect of Mg doping on electrochemical characteristics of the LiMn_{0.8}Fe_{0.2}PO₄. The corresponding curves for both materials, run at a rate of 0.1C are shown in Fig. 3a. (A) LiMn_{0.8}Fe_{0.2}PO₄ /SGCNT shows typical two plateaus corresponding to the redox of Fe²⁺/Fe³⁺ (3.5 V vs. Li/Li⁺) and Mn²⁺/Mn³⁺ (4.1 V vs. Li/Li⁺). The total reversible capacity of the Fe and Mn phases was 106 mA h g⁻¹ per composite,

corresponding to the 125 mA h g⁻¹ for pure LiMn_{0.8}Fe_{0.2}PO₄ after subtracting the capacity attributed to SGCNT (see Fig. S5) in the composite. The value of 134 mA h g⁻¹ is comparable to the 120-140 mA h g⁻¹ range reported elsewhere. $^{54-56}$

1 atomic % of Mg-doping improved the reversible capacity of LiMn_{0.8}Fe_{0.2}PO₄ to 115 mA h g⁻¹ per composite as shown in Fig. 3a. This value corresponds to 146 mA h g⁻¹ for pure LiMn_{0.792}Fe_{0.198}Mg_{0.010}PO₄, which is 84% of its theoretical capacity. Furthermore, the Mn²⁺/Mn³⁺ redox plateau is 1.1 times pronounced in the doped sample, while the plateaus for Fe²⁺/Fe³⁺ shows no change, suggesting that the addition of Mg facilitated the lithiation/delithiation in the Mn_{0.8}PO₄ phase.

The charge-discharge profiles were then converted to graphs of differential capacity (dO/dE) with respect to voltage (Fig. 3b) in order to compare the number of electrons transferred during Fe²⁺/Fe³⁺ and Mn²⁺/Mn³⁺ redox between two composites. Overall, the electron transferred for the Mn²⁺/Mn³⁺ redox improved from (A) 0.60e⁻ to (B) 0.66e⁻ after Mg doping, while that for Fe²⁺/Fe³⁺ redox remains constant at 0.19e. This indicates that 82% of Mn species for the LiMn_{0.792}Fe_{0.198}Mg_{0.010}PO₄/SGCNT participate in lithiation/delithiation, while Li⁺ in the Fe site react almost 100% for both samples. In addition, the inset in Fig. 3b shows a narrowing peak of separation for the Mn²⁺/Mn³⁺ reaction due to Mg doping, with the values from 94 to 89 mV, at the same time, virtually no change was observed for Fe²⁺/Fe³⁺ reaction. This 5 mV drop indicates that improved Li⁺ diffusion, which likely results from two effects of Mg addition. First, the unreactive Mg_{0.010}PO₄ phase can act as a buffer against volume retraction and lattice collapse that may results from changes in Fe and Mn diameters during oxidation. This is often referred as the "pillar effect," ⁵⁷ and minimizes the disruption to the Li⁺ conduction path by decreasing distortion at the boundary of the bc plane. The calculated percentages of bc-plane misfit and volume change during lithiation-delithiation support these ideas. As shown in Table 1, the former decrease from 2.46 to 2.29% by Mg doping, while the latter decreases from 9.65 to 9.29 %. It is well known that the diffusion of Li⁺ in the crystal of phosphor-olivine compounds (LiMPO₄; M = Mn, Fe, Co, and Ni) is the 1-D diffusion with b-axis direction during its two-phase reaction of LiMPO₄/MPO₄. Additionally, Li⁺ insertion/extraction may preferentially occur at the phase boundary of the reaction, which runs parallel to the bc plane. 58 Therefore, reducing discontinuity along the bc plane may lead to smoother two-phase reactions of LiMn_{0.8}Fe_{0.2}PO₄. ⁵⁹ Because Mg²⁺ does not change valence states during lithiation/delithiation, the presence of the $Mg_{0.01}PO_4$ phase likely buffers the misfit along the bc plane, aiding in improved electrochemical performance. Secondly, the presence of the unreacted Li⁺ surrounded

by Mg^{2^+} accelerates Li^+ transfer by destabilizing $Mn_{0.8}PO_4$ phase with the repulsion between Mn^{3^+} - Li^+ , often referred as "nucleation enhancer". Note that the observed peak-separation decrease can also result from improved electrical conductivity as well, which can be accounted for the increased number of holes generated by Mg-doping in the n-type $LiMn_{0.8}Fe_{0.2}PO_4$. These effects will be further studied using x-ray photoelectron spectroscopy (XPS) and electrochemical impedance spectroscopy (EIS).

Mg $2p_{3/2}$, Fe $2p_{3/2}$, and Mn $2p_{3/2}$ XPS measurements were then carried out in order to investigate the valence states of the three metal ions, in LiMn_{0.792}Fe_{0.198}Mg_{0.010}PO₄ both at delithiated (4.5 V) and lithiated (2.5 V) states. Looking at the spectra for Mn $2p_{3/2}$ and Fe $2p_{3/2}$ firstly, peaks for both of Mn and Fe shift with lithiation of LiMn_{0.792}Fe_{0.198}Mg_{0.010}PO₄/SGCNT composites; from 642.5 to 642.0 eV for the Mn $2p_{3/2}$, and from 713.2 to 711.5 eV for the Fe $2p_{3/2}$. These shifts for the Mn $2p_{3/2}$ and Fe $2p_{3/2}$ correspond to the shift of Mn²⁺/Mn³⁺⁶¹ and Fe²⁺/Fe³⁺,⁶² respectively. These results show the reversible redox couple of Mn and Fe ions for the LiMn_{0.792}Fe_{0.198}Mg_{0.010}PO₄/SGCNT. On the other hand, the peak tops of Mg $2p_{3/2}$ spectra remain at the same binding energy (48.1 eV), indicating the existence of completely inert Mg²⁺ through the lithiation and delithiation process between 2.5 and 4.5 V vs. Li/Li⁺. This unreacted Mg²⁺ supports the possible existence of Mg_{0.010}PO₄ phase, which can provide the "pillar effect" and act as "nucleation enhancer". ^{34, 59, 63}

[Ultrafast Behavior and its Origins]

Charge-discharge tests at variable current densities were performed in order to study the influence of Mg doping on the lithiation/delithiation at Fe_{0.2}PO₄ and Mn_{0.8}PO₄ phases. Fig. 4a shows the discharge profiles for (A) LiMn_{0.8}Fe_{0.2}PO₄ /SGCNT at current densities ranging from 0.1C to 50C. Mn³⁺/Mn²⁺ and Fe³⁺/Fe²⁺ plateaus are clearly visible at 4.1 V and 3.5V, respectively, at the lowest rate. As current density increases from 0.1C to 5C, discharge capacity slowly decreases from 100 to 78 mA h g⁻¹, yet the Mn and Fe plateaus remain somewhat visible. However, as the current density increases further to 10C, the two plateaus effectively disappear. That being said, (A) LiMn_{0.8}Fe_{0.2}PO₄ /SGCNT maintains a discharge capacity of 38 mA h g⁻¹ per composite even at 50C, corresponding to 36 % retention from the lowest current density: this value surpasses most of those previously reported for similar LiMn_xFe_{1-x}PO₄ compounds. ^{64,65} This impressive performance results from a combination of several factors. Again, the shortened Li⁺ diffusion path length due to the decrease particle size likely plays a role, as does the increased surface area of the active material due to dispersion of nanoparticles throughout the

highly conductive SGCNT matrix.

Fig. 4b shows that Mg doping further improved the rate capability of LiMn_{0.8}Fe_{0.2}PO₄/SGCNT composite with the visible difference even at low current densities. In particular, the discharge curve for LiMn_{0.792}Fe_{0.198}Mg_{0.010}PO₄/SGCNT at 0.1 C shows a Mn plateau at 4.1 V that is 1.1 times longer than for the undoped composite. Increasing current densities to 5C results in similar changes to the discharge curves, with the difference in capacity attributed to Mn becoming even more pronounced; however, the doped sample shows a discharge capacity of 94 mA h g⁻¹ per composite, an improvement of 1.2 times over undoped sample. The effect is even more pronounced at 50C: the measured discharge capacity of 54 mA h g⁻¹ per composite corresponds to a 47% retention of capacity over 0.1C and improvements of 1.4 times over undoped sample. Overall, these results provide further evidence for improved Li diffusion and electrical conductivity. The results for both samples are summarized in Fig. 4c. The rate capability for our $LiMn_{0.792}Fe_{0.198}Mg_{0.010}PO_4/SGCNT$ is the one of the highest among the reported LiMn_{0.8}Fe_{0.2}PO₄. ⁶⁴⁻⁶⁶ Such high rate capability is comparable to those for other cathode materials such as LiCoO₂ (= 50C; charged and discharged in the voltage range from 3.0 to 4.5 V. The electrode composed of 80 wt% of active material, 10 wt% of conductive carbon, and 10 wt% of binder.), ⁶⁷ LiMn₂O₄ (= 60C; charged and discharged in the voltage range from 3.0 to 4.3 V.). 68 LiFePO₄ (= 60C; charged and discharged in the voltage range from 2.0 to 4.3 V. The electrode composed of 83 wt% of active material, 12 wt% of conductive carbon, and 5 wt% of binder. The loading mass of the electrode is 5 mg cm⁻².), ⁶⁹ and Li₃V₂(PO₄)₃ (= 100C; charged and discharged in the voltage range from 2.0 to 4.3 V. The electrode composed of 80 wt% of active material, 10 wt% of conductive carbon, and 10 wt% of binder. The loading mass of the electrode is 1.6-2.0 mg cm⁻².)⁷⁰. Note that the weight of the electrode is naturally dependent upon the electrode thickness, the state of charge, the voltage ranges. Therefore, we picked up the highest-achieved rate capability to compare with our composites. It should be also mentioned that the LiMn_{0.8}Fe_{0.2}PO₄ has the lowest electric conductivity (= 10^{-14} - 10^{-15} Ω^{-1} cm⁻¹) and ionic conductivity (= 10^{-15} - 10^{-17} cm² s⁻¹) compare to the other cathode materials, which is the large handicap to achieve high rate-capability.

Next, the mechanism by which performance improved due to Mg doping was further explored using EIS measurements; the corresponding spectra for the blocking cells containing either $LiMn_{0.8}Fe_{0.2}PO_4/SGCNT$ or $LiMn_{0.792}Fe_{0.198}Mg_{0.010}PO_4/SGCNT$ are shown in Fig. 5a. The spectra for the two samples are both semicircular in the high to medium frequency region, an effect can be attributed to charge transfer resistance (R_{ct}) at different interfaces, such as

between the current collector and the composites, grain boundaries of composites, and between the electrolyte and composite surface. Assuming that the nanoparticles size and the composite morphology are same with or without Mg dopant (see Fig. 2 and Fig. S3), the difference of R_{ct} between two samples resulted from the first and the second. The diameter of the semicircle, which is proportional to R_{ct} , is significantly smaller for the doped sample than it is for the undoped one. The exact values were evaluated by fitting the EIS semicircular spectra with the equivalent circuit (Fig. 5a inset); the fitted results are shown in Table 2. Overall, Mg doping resulted in a 50% drop in R_{ct} , which is in good agreement with the previous results in the dQ/dE section showing a decrease in peak potential separation.

Additional EIS measurements for the Li half cells were completed to track changes in the lithium diffusion coefficient (D_{Li}) at the voltage around the Fe plateau (Fig. 5b) and the Mn plateau (Fig. 5c). D_{Li} was calculated using the following equation: $D_{Li} = 0.5 R^2 T^2 / S^2 n^4 F^4 C^2 \sigma^2$, where R is the gas constant, T is temperature, S is the surface area of the electrode, n is the number of electrons per molecule during oxidization, F is the Faraday constant, C is the concentration of Li^+ , and σ is the Warburg-impedance coefficient of the material. Detailed explanation of the D_{Li} calculations are described in the caption of Table 2.

The calculated D_{Li} values for the two composites (A) and (B) are shown in Table 2. The doped sample shows a much higher D_{Li} in the Fe site (3.5 V) and the Mn site (4.1 V) than both the undoped one and previous reports for $LiMn_xFe_{1-x}PO_4$ (1.0 × 10⁻¹⁶ cm² s⁻¹).⁷¹ This increase can again be explained by the pillar effect,⁵⁷ as well as by the enhancement of Li^+ intercalation within the $Mg_{0.01}PO_4$ phase due to nucleation.⁴⁸

Cycle-life testing revealed that LiMn_{0.792}Fe_{0.198}Mg_{0.01}PO₄/SGCNT delivered a capacity of 100 mA h g⁻¹ after 3,000 cycles at 1C, corresponding to an 84% capacity retention (Fig. 6). The initial coulobmic efficiency was 97% with the irreversible capacity of 3.6 mAh g⁻¹ per composite, which can be due to the irreversible oxidation reaction of the electrolyte on the surface of SGCNT (30wt% in the composite) during initial cycling as shown in the supporting information Fig. S1. Then, the coulombic efficiency increases to over 99.1 % after 5th cycle and was maintained until 3,000th cycle. The stabilization of the cycling performance can be due to the passivation on the active site of SGCNT by the oxidative decomposition product of the electrolyte (possibly SEI film). The detailed charge-discharge profiles for a selection of cycles are shown in the inset of Fig. 6. No obvious signs of voltage drop or capacity loss from the Fe²⁺/Fe³⁺ redox system are visible; however, the reversible capacity of the Mn²⁺/Mn³⁺ system starts to decrease after 500 cycles, which may result from dissolution of Mn²⁺ by Jahn-Teller

lattice deformation. This possibility is being tested by searching for Mn²⁺ in the electrolyte using inductively coupled plasma emission spectroscopy, and/or by stabilizing Mn through the additional doping of other metal ions.

Conclusion

Spherical LiMn_{0.792}Fe_{0.198}Mg_{0.010}PO₄ nanocrystals (10-40 nm ϕ) were successfully embedded between unbundled interstices of supergrowth (single-walled) carbon nanotubes (SGCNT) *via* UC treatment and the subsequent short-duration heat treatment. The synthesized single-cryistalline LiMn_{0.792}Fe_{0.198}Mg_{0.010}PO₄ nanospheres are directly attached on the surface of highly electric-conductive SGCNT. Structural and electrochemical testing showed that 1.0 atom% of Mg doping into the nano-sized LiMn_{0.8}Fe_{0.2}PO₄ solid-solution enhanced its electric conductivity (50% decrease of R_{ct}) and Li⁺ diffusivity (200% increase of D_{Li}) resulting in the ultrafast Li⁺ migration. These improved properties yielded a potential new lithium storage material with an excellent rate performance of 54 mA h g⁻¹ per composite (corresponding to 77 mA h g⁻¹ per pure LiMn_{0.792}Fe_{0.198}Mg_{0.010}PO₄) at 50C and a superb cycle stability of 84% retention of the initial capacity after 3,000 cycles.

Acknowledgements

The authors are indebted to K. Hata, AIST Japan and S. Iijima (Meijo University, Japan) for variable discussions on SGCNT through NEDO project Carbon Nanotube Capacitor Project (2006-2011).

Reference

- A. K. Padhi, K. S. Nanjundaswamy and J. B. Goodenough, J. Electrochem. Soc., 1997, 144, 1188-1194.
- 2. G. H. Li, H. Azuma and M. Tohda, Electrochem. Solid-State Lett., 2002, 5, A135-A137.
- 3. K. Amine, H. Yasuda and M. Yamachi, Electrochem. Solid-State Lett., 2000, 3, 178-179.
- 4. O. Garcia-Moreno, M. Alvarez-Vega, F. Garcia-Alvarado, J. Garcia-Jaca, J. M. Gallardo-Amores, M. L. Sanjuan and U. Amador, *Chem. Mater.*, 2001, **13**, 1570-1576.
- 5. O. K. Park, Y. Cho, S. Lee, H.-C. Yoo, H.-K. Song and J. Cho, *Energy Environ. Sci.*, 2011, 4, 1621.
- C. Delacourt, L. Laffont, R. Bouchet, C. Wurm, J. B. Leriche, M. Morcrette, J. M. Tarascon and C. Masquelier, *J. Electrochem. Soc.*, 2005, 152, A913-A921.
- 7. G. Kobayashi, S. Nishimura, M.-S. Park, R. Kanno, M. Yashima, T. Ida and A. Yamada, *Adv. Funct. Mater.*, 2009, 19, 395-403.

- 8. D. Morgan, A. Van der Ven and G. Ceder, Electrochem. Solid-State Lett., 2004, 7, A30-A32.
- 9. B. Ellis, L. K. Perry, D. H. Ryan and L. F. Nazar, J. Am. Chem. Soc., 2006, 128, 11416-11422.
- 10. F. Cheng, W. Wan, Z. Tan, Y. Huang, H. Zhou, J. Chen and X. Zhang, *Electrochim. Acta*, 2011, **56**, 2999-3005.
- 11. H. Li and H. Zhou, Chem. Commun., 2012, 48, 1201-1217.
- 12. X. Zhou, F. Wang, Y. Zhu and Z. Liu, J. Mater. Chem., 2011, 21, 3353.
- 13. http://www.a123systems.com/lifepo4-battery-cell.htm
- 14. V. Etacheri, R. Marom, R. Elazari, G. Salitra and D. Aurbach, *Energy Environ. Sci.*, 2011, 4, 3243-3262.
- M. Yonemura, A. Yamada, Y. Takei, N. Sonoyama and R. Kanno, J. Electrochem. Soc., 2004, 151, A1352-A1356.
- Y. B. Cao, J. G. Duan, G. R. Hu, F. Jiang, Z. D. Peng, K. Du and H. W. Guo, *Electrochim. Acta*, 2013, 98, 183-189.
- 17. N. S. Norberg and R. Kostecki, J. Electrochem. Soc., 2012, 159, A1431-A1434.
- 18. N. N. Bramnik and H. Ehrenberg, J. Alloys Compd., 2008, 464, 259-264.
- 19. G. H. Li, H. Azuma and M. Tohda, J. Electrochem. Soc., 2002, 149, A743-A747.
- C. Hu, H. Yi, H. Fang, B. Yang, Y. Yao, W. Ma and Y. Dai, *Electrochem. Commun.*, 2010, 12, 1784-1787.
- 21. J. Kim, K. Y. Park, I. Park, J. K. Yoo, J. Hong and K. Kang, *J. Mater. Chem.*, 2012, **22**, 11964-11970.
- 22. A. Yamada, Y. Kudo and K. Y. Liu, J. Electrochem. Soc., 2001, 148, A1153-A1158.
- 23. L. Chen, Y.-Q. Yuan, X. Feng and M.-W. Li, J. Power Sources, 2012, 214, 344-350.
- 24. B. Zhang, X. J. Wang, H. Li and X. J. Huang, J. Power Sources, 2011, 196, 6992-6996.
- 25. J. K. Kim, G. S. Chauhan, J. H. Ahn and H. J. Ahn, J. Power Sources, 2009, 189, 391-396.
- G. Meligrana, F. Di Lupo, S. Ferrari, M. Destro, S. Bodoardo, N. Garino and C. Gerbaldi, *Electrochim. Acta*, 2013, 105, 99-109.
- 27. K. Kagesawa, E. Hosono, M. Okubo, D. Nishio-Hamane, T. Kudo and H. Zhou, *J. Power Sources*, 2014, **248**, 615-620.
- 28. W. Liu, P. Gao, Y. Mi, J. Chen, H. Zhou and X. Zhang, J. Mater. Chem. A, 2013, 1, 2411-2417.
- 29. W. Ojczyk, J. Marzec, J. Dygas, F. Krok, R. S. Liu and J. Molenda, *Materi. Sci.-Poland*, 2006, 24, 103-113.
- J. Yoshida, M. Stark, J. Holzbock, N. Huesing, S. Nakanishi, H. Iba, H. Abe and M. Naito, J. Power Sources, 2013, 226, 122-126.
- K. Du, L. H. Zhang, Y. B. Cao, H. W. Guo, Z. D. Peng and G. R. Hu, *J. Appl. Electrochem.*, 2011, 41, 1349-1355.
- 32. K. Y. Park, J. Hong, J. Kim, Y. U. Park, H. Kim, D. H. Seo, S. W. Kim, J. W. Choi and K. Kang, *J. Electrochem. Soc.*, 2013, **160**, A444-A448.
- 33. S. S. Das, N. P. Singh, V. Srivastava and P. K. Srivastava, Ionics, 2008, 14, 563-568.

- 34. J. Kim, Y.-U. Park, D.-H. Seo, J. Kim, S.-W. Kim and K. Kang, *J. Electrochem. Soc.*, 2011, **158**, A250-A254.
- G. Yang, H. Ni, H. Liu, P. Gao, H. Ji, S. Roy, J. Pinto and X. Jiang, J. Power Sources, 2011, 196, 4747-4755.
- 36. J. Ni and L. Gao, J. Power Sources, 2011, 196, 6498-6501.
- 37. T. Shiratsuchi, S. Okada, T. Doi and J.-i. Yamaki, Electrochim. Acta, 2009, 54, 3145-3151.
- 38. N. Jayaprakash, N. Kalaiselvi and P. Periasamy, Int. J. Electrochem. Sci., 2008, 3, 476-488.
- 39. D. Jang, K. Palanisamy, J. Yoon, Y. Kim and W. S. Yoon, J. Power Sources, 2013, 244, 581-585.
- 40. H. Wang, Y. Yang, Y. Liang, L.-F. Cui, H. S. Casalongue, Y. Li, G. Hong, Y. Cui and H. Dai, *Angew. Chem. Int. Ed.*, 2011, **50**, 7364-7368.
- 41. K. Hata, D. N. Futaba, K. Mizuno, T. Namai, M. Yumura and S. Iijima, Sci, 2004, 306, 1362-1364.
- 42. A. Izadi-Najafabadi, D. N. Futaba, S. Iijima and K. Hata, *J. Am. Chem. Soc.*, 2010, **132**, 18017-18019.
- 43. K. Naoi, S. Ishimoto, N. Ogihara, Y. Nakagawa and S. Hatta, *J. Electrochem. Soc.*, 2009, **156**, A52-A59.
- 44. K. Naoi, W. Naoi, S. Aoyagi, J. Miyamoto and T. Kamino, Acc. Chem. Res., 2012, 46, 1075-1083.
- 45. K. Naoi, S. Ishimoto, Y. Isobe and S. Aoyagi, J. Power Sources, 2010, 195, 6250-6254.
- 46. K. Kisu, M. Iijima, E. Iwama, M. Saito, Y. Orikasa, W. Naoi and K. Naoi, J. Mater. Chem. A, 2014.
- 47. K. Naoi, D. Yonekura, S. Moriyama, H. Goto, E. Iwama, S. Kubota, S. Ishimoto and W. Naoi, *J. Alloys Compd.*, 2014, **605**, 137-141.
- 48. M. Akoshima, K. Hata, D. N. Futaba, K. Mizuno, T. Baba and M. Yumura, *Jpn. J. Appl. Phys.*, 2009, 48, 05EC07.
- 49. K. Naoi, S. Ishimoto, J. Miyamoto and W. Naoi, Energy Environ. Sci., 2012, 5, 9363-9373.
- 50. B. Gao, C. Peng, G. Z. Chen and G. L. Puma, Appl. Catal., B., 2008, 85, 17-23.
- 51. B. Z. Li, Y. Wang, L. Xue, X. P. Li and W. S. Li, J. Power Sources, 2013, 232, 12-16.
- 52. V. C. Moore, M. S. Strano, E. H. Haroz, R. H. Hauge, R. E. Smalley, J. Schmidt and Y. Talmon, *Nano Lett.*, 2003, **3**, 1379-1382.
- 53. S. Sakurai, F. Kamada, D. N. Futaba, M. Yumura and K. Hata, Nanoscale Res. Lett., 2013, 8.
- 54. F. Ye, L. Wang, X. He, M. Fang, Z. Dai, J. Wang, C. Huang, F. Lian, J. Wang, G. Tian and M. Ouyang, *J. Power Sources*, 2014, **253**, 143-149.
- 55. T. Liu, B. Wu and X. Wu, Solid State Ionics, 2014, 254, 72-77.
- T. T. D. Nguyen, L. Dimesso, G. Cherkashinin, J. C. Jaud, S. Lauterbach, R. Hausbrand and W. Jaegermann, *Ionics*, 2013, 19, 1229-1240.
- 57. H. Liu, Q. Cao, L. J. Fu, C. Li, Y. P. Wu and H. Q. Wu, Electrochem. Commun., 2006, 8, 1553-1557.
- 58. G. Y. Chen, X. Y. Song and T. J. Richardson, Electrochem. Solid-State Lett., 2006, 9, A295-A298.
- N. Meethong, H. Y. S. Huang, S. A. Speakman, W. C. Carter and Y. M. Chiang, *Adv. Funct. Mater.*, 2007, 17, 1115-1123.
- 60. Y. Yang, K. Li and H. Li, Int. J. Appl. Ceram. Technol., 2013, 1-6.

- 61. Y. Huang, J. Fang, F. Omenya, M. O'Shea, N. A. Chernova, R. Zhang, Q. Wang, N. F. Quackenbush, L. F. J. Piper, D. O. Scanlon and M. S. Whittingham, *J. Mater. Chem. A*, 2014, **2**, 12827-12834.
- 62. S. T. Myung, S. Komaba, N. Hirosaki, H. Yashiro and N. Kumagai, *Electrochim. Acta*, 2004, **49**, 4213-4222.
- 63. V. Ramar and P. Balaya, Phys. Chem. Chem. Phys., 2013, 15, 17240-17249.
- 64. B. Ding, G. Ji, Y. Ma, P. F. Xiao, L. Lu and J. Y. Lee, J. Power Sources, 2014, 247, 273-279.
- 65. K. Saravanan, V. Ramar, P. Balaya and J. J. Vittal, J. Mater. Chem., 2011, 21, 14925-14935.
- S. K. Martha, J. Grinblat, O. Haik, E. Zinigrad, T. Drezen, J. H. Miners, I. Exnar, A. Kay, B. Markovsky and D. Aurbach, *Angewandte Chemie-International Edition*, 2009, 48, 8559-8563.
- 67. Q. Hao, H. Ma, Z. Ju, G. Li, X. Li, L. Xu and Y. Qian, Electrochim. Acta, 2011, 56, 9027-9031.
- C. L. Chen, K. F. Chiu, Y. R. Chen, C. C. Chen, H. C. Lin and H. Y. Chiang, *Thin Solid Films*, 2013, 544, 182-185.
- 69. Y. G. Wang, Y. R. Wang, E. J. Hosono, K. X. Wang and H. S. Zhou, *Angewandte Chemie-International Edition*, 2008, **47**, 7461-7465.
- 70. C. Wang, W. Shen and H. Liu, New J. Chem., 2014, 38, 430-436.
- 71. A. M. Hashambhoy and J. F. Whitacre, J. Electrochem. Soc., 2011, 158, A390-A395.

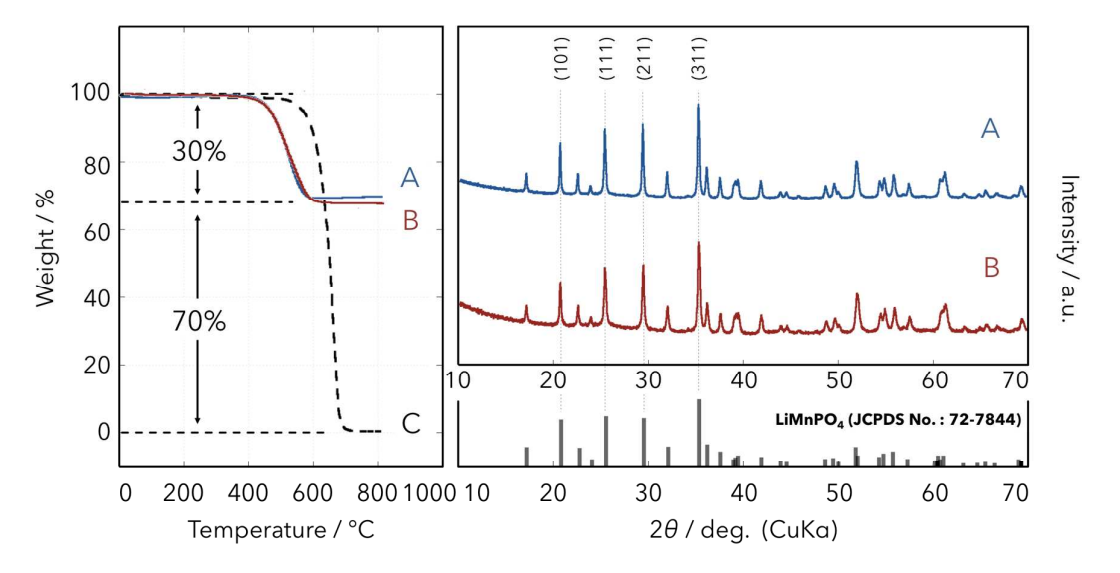


Fig. 1 **[Left]** TGA curves for (A) LiMn_{0.8}Fe_{0.2}PO₄/SGCNT, (B) LiMn_{0.792}Fe_{0.198}Mg_{0.010}PO₄ /SGCNT, and (C) the pristine SGCNT. TGA measurements were performed under synthetic air starting at room temperature and increasing to 800°C at a rate of 10°C min⁻¹. The ratio of SGCNT (decreased weight ratio up to 800°C) were typically 30 wt% with an error factor of 2% both for composites (A) and (B), which are consistent with the initial dosage (see the experimental section for more details of the dosage). **[Right]** XRD patterns for (A) LiMn_{0.8}Fe_{0.2}PO₄/SGCNT, (B) LiMn_{0.792}Fe_{0.198}Mg_{0.010}PO₄/SGCNT, and a reference LiMnPO₄ (JCPDS card No 72-7844). The major diffraction peaks of these composites ((101), (111), (211), and (301)) are well indexed to the orthorhombic structure of LiMnPO₄. No peaks for possible impurities were found both in the patterns for composites (A) and (B).

Table 1. XRD-derived crystallographic parameters for (A) LiMn_{0.8}Fe_{0.2}PO₄/SGCNT, (A') Mn_{0.8}Fe_{0.2}PO₄/SGCNT (delithiated composite A), (B) LiMn_{0.792}Fe_{0.198}Mg_{0.010}PO₄/SGCNT, (B') Mn_{0.792}Fe_{0.198}Mg_{0.010}PO₄/SGCNT (delithiated composite B), and (C) a reference LiMn_{0.8}Fe_{0.2}PO₄. The percentage of the bc-phase misfit between lithiation and delithiation was calculated from the tabled b- and c- parameters; anamely, misfit (%) = $[1-(b^*c^*)/(b^*c)]*100$. Volume change was calculated from volume change (%) = $(a^*b^*c^*)/(a^*b^*c)*100$.

| | Sample | S. G. | a (Å) | b (Å) | c (Å) | V (ų) | bc plane misfit / % | Volume change / % |
|----|--|-------|---------|--------|--------|--------|------------------------|----------------------|
| Α | LiMn _{0.8} Fe _{0.2} PO ₄ | Pnma | 10.4216 | 6.0822 | 4.7349 | 300.13 | 0.47 | 0.45 |
| A' | $\mathrm{Mn_{0.8}Fe_{0.2}PO_{4}}$ | Pnma | 9.6510 | 5.8820 | 4.7770 | 271.18 | 2.46 | 9.65 |
| В | LiMn _{0.792} Fe _{0.198} Mg _{0.01} PO ₄ | Pnma | 10.4192 | 6.0881 | 4.7344 | 299.97 | 2.29 | 9.29 |
| B′ | $Mn_{0.792}Fe_{0.198}Mg_{0.01}PO_4$ | Pnma | 9.6700 | 5.8876 | 4.7792 | 272.09 | 2.29 | 7.27 |
| С | LiMn _{0.8} Fe _{0.2} PO ₄ (Ref.) ⁵¹⁾ | Pnma | 10.4233 | 6.0812 | 4.7320 | 299.94 | | |

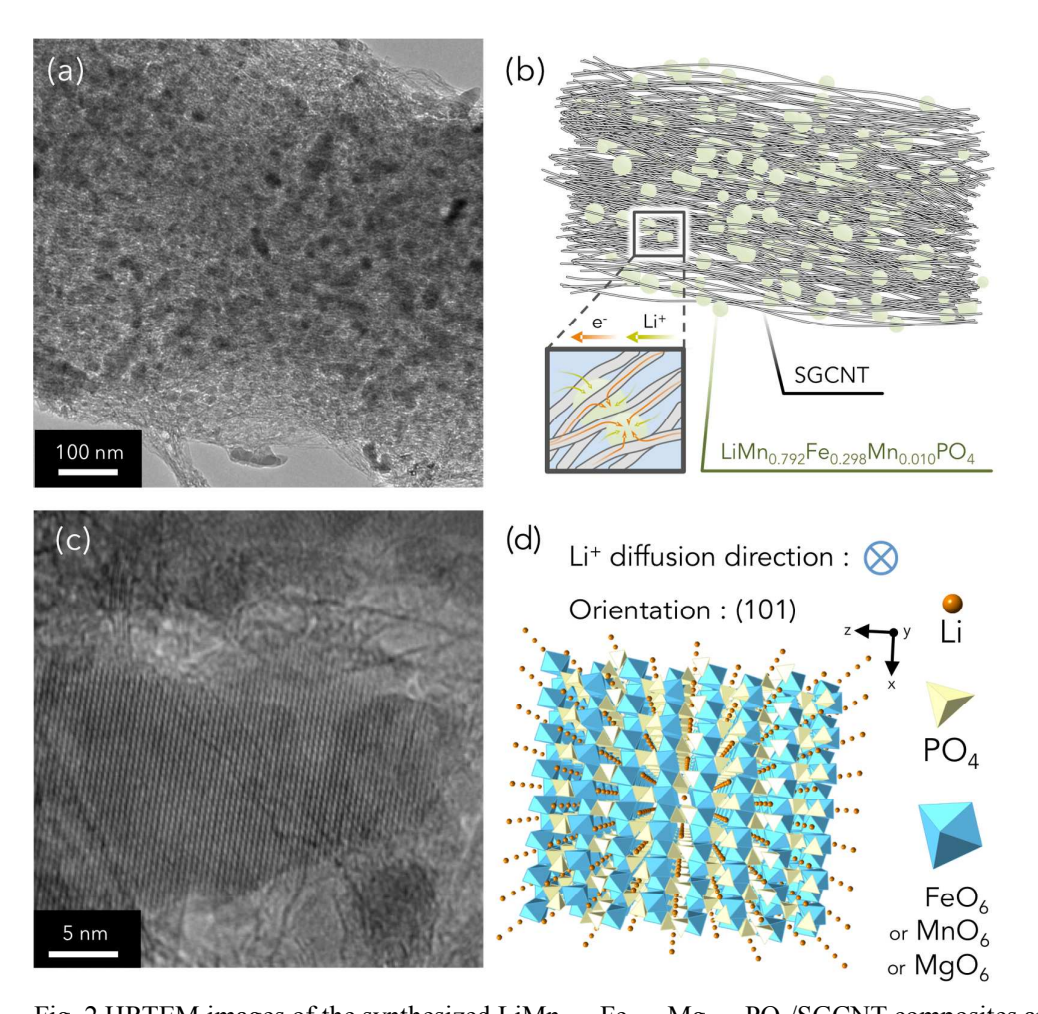


Fig. 2 HRTEM images of the synthesized LiMn_{0.792}Fe_{0.198}Mg_{0.010}PO₄/SGCNT composites and their corresponding schematic illustrations. (a) Lower magnification HRTEM image of LiMn_{0.792}Fe_{0.198}Mg_{0.010}PO₄/SGCNT composites to observe all over the composite structure, suggesting that the spherical LiMn_{0.792}Fe_{0.198}Mg_{0.010}PO₄ are highly dispersed and encapsulated within the SGCNT interstices. (b) Schematic of Fig. 2 (a) demonstrating improved Li⁺ and electron path of the encapsulated LiMn_{0.792}Fe_{0.198}Mg_{0.010}PO₄ nanoparticles. (c) Magnified HRTEM image of the LiMn_{0.792}Fe_{0.198}Mg_{0.010}PO₄ nanoparticles (10-40 nm) attached to the SGCNT surface, demonstrating a clear crystal lattice aligned along the (101) plane. (d) 3D graphic image of a LiMn_{0.792}Fe_{0.198}Mg_{0.010}PO₄ nanocrystal with the direction of Li⁺ diffusion illustrated by CrystalMaker (Crystalmaker software Ltd.).

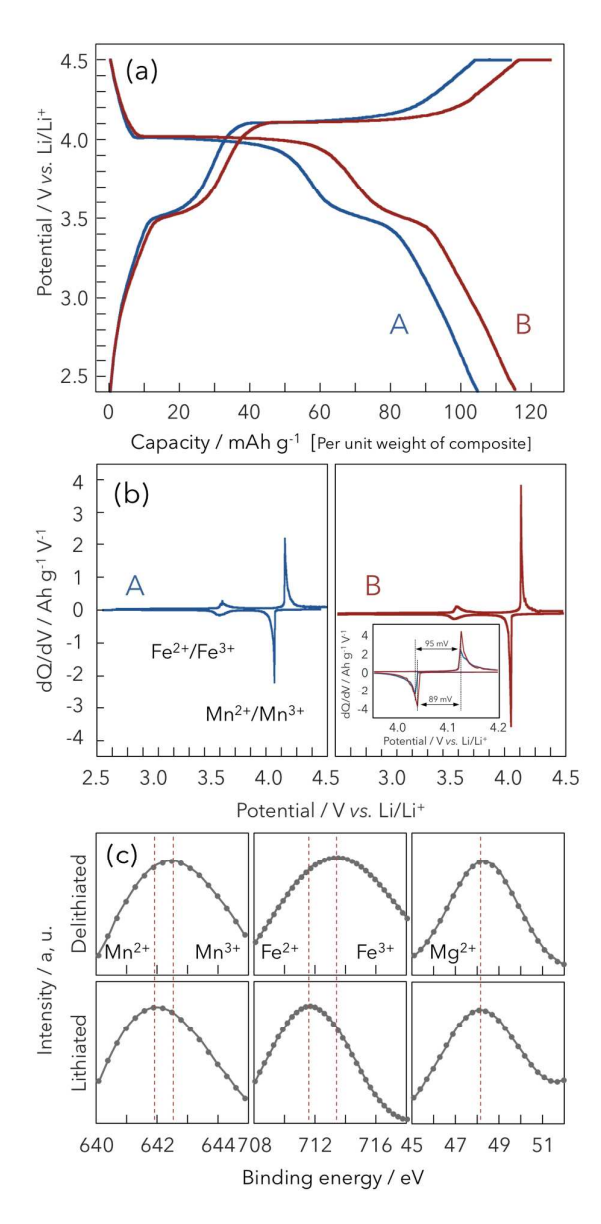


Fig. 3 (a) Charge-discharge curves for (A) LiMn_{0.8}Fe_{0.2}PO₄/SGCNT and (B)

LiMn_{0.792}Fe_{0.198}Mg_{0.010}PO₄/SGCNT composites. Charge-discharge tests were performed using a half cells with Li and composite electrodes (A) or (B). Used electrolyte composition was 1M LiPF₆ /EC + DEC (EC/DEC =50/50, v/v). Tested condition was under the CC-CV (charge) and CC (discharge) mode between 2.5 and 4.5 V at a current density of 17 mA g⁻¹ (corresponding to 0.1C). (b) Differential capacity (dQ/dV) with respect to potential for composites (A) and (B), derived from the corresponding charge-discharge curves shown in Fig. 3 (a). The inset highlights the peak voltage separations for Mn²⁺/Mn³⁺ redox for composites A and B. (c) XPS spectra for Mg 2p_{3/2}, Fe 2p_{3/2}, and Mn 2p_{3/2} for LiMn_{0.792}Fe_{0.198}Mg_{0.010}PO₄/SGCNT in both

delithiated (at 4.5V vs. Li/Li⁺) and lithiated (at open-circuit voltage) states.

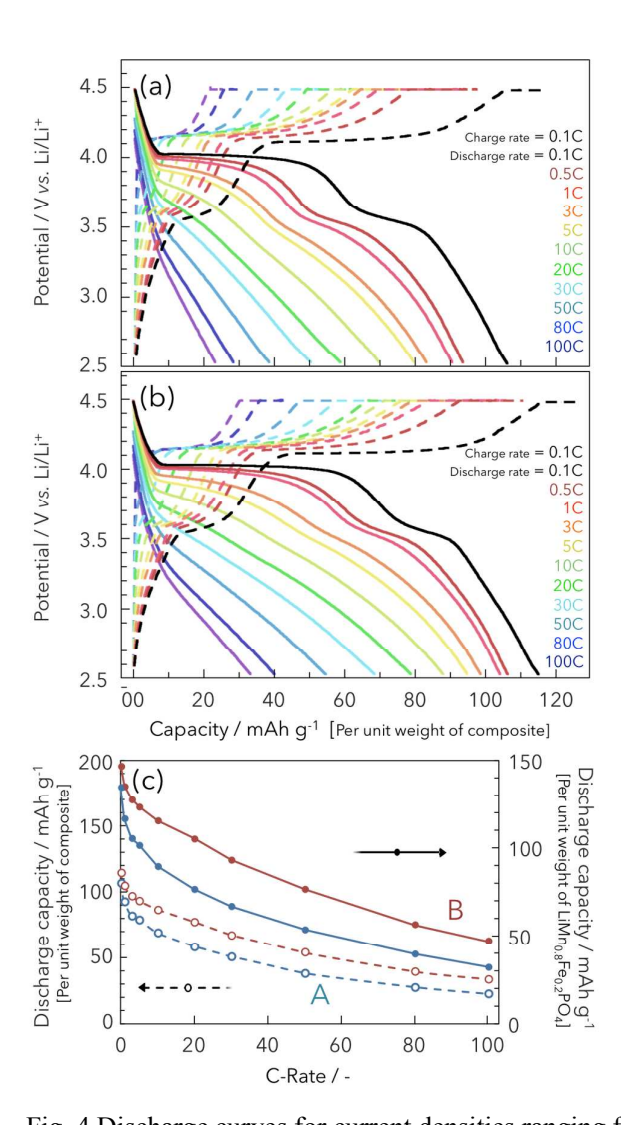


Fig. 4 Discharge curves for current densities ranging from 0.1C to 100C for (a) LiMn_{0.8}Fe_{0.2}PO₄/SGCNT and (b) LiMn_{0.792}Fe_{0.198}Mg_{0.010}PO₄/SGCNT, along with the charge curves for the current density at 0.1 C. In both cases, typical two plateaus attributed for Fe²⁺/Fe³⁺ and Mn²⁺/Mn³⁺ are clearly observed at the slowest 0.1C. (c) Discharge capacity with respect to current density for (A, blue) LiMn_{0.8}Fe_{0.2}PO₄/SGCNT and (B, red) LiMn_{0.792}Fe_{0.198}Mg_{0.010}PO₄/SGCNT. Broken lines correspond to the capacity per composite, and the solid lines correspond to the capacity per pure LiMn_{0.8(1-z)}Fe_{0.2(1-z)}Mg_zPO₄ (z = 0 or 0.01) after subtracting the capacity attributed to SGCNT (see Fig. S5) in the composite. Test conditions were identical to those used in Fig. 3.

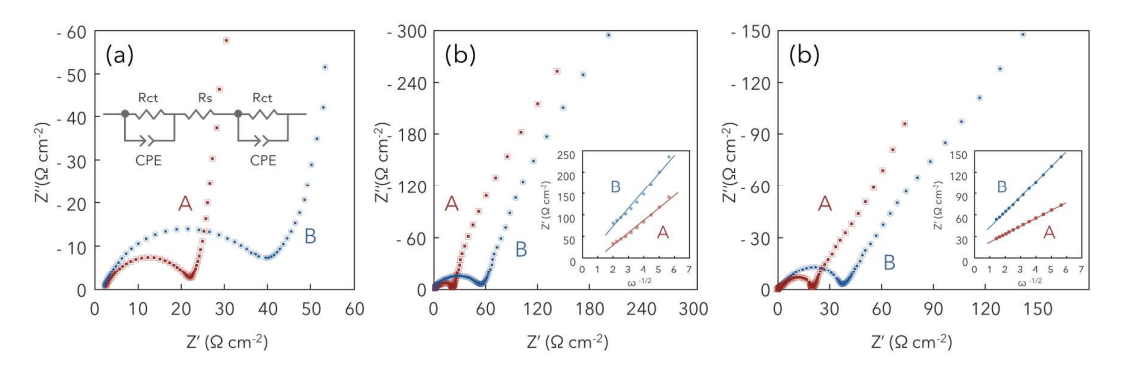


Fig. 5 Electrochemical impedance spectroscopy (EIS) data for the (A) LiMn_{0.8}Fe_{0.2}PO₄/SGCNT (blue spheres) and (B) LiMn_{0.792}Fe_{0.198}Mg_{0.010}PO₄/SGCNT (red squares) composites. (a) Nyquist plots for the blocking cells tested at open-circuit voltage and consisting of two identical electrodes separated by a 25 μm separator. Use electrolyte composition was 1 M LiPF₆/EC+DEC (EC/DEC =50/50, v/v). (b) Nyquist plots for half cells tested at 3.5 V vs. Li/Li⁺ corresponds to the plateau of Fe²⁺/Fe³⁺ redox and utilizing a Li electrode and a composite electrode separated by a 25 μm separator. Before starting EIS measurements, the cell voltage was held at 3.5 V vs. Li/Li⁺ for 20 min until the current dropped to an equilibrium level below 1 μA cm⁻². Frequency was scanned over 0.01 Hz–100 kHz, while amplitude was set to 5 mV. (c) Nyquist plots for half cells tested at 4.1 V vs. Li/Li⁺ which corresponds to the plateau of Mn²⁺/Mn³⁺ redox. Tested conditions were identical to those for Fig. 5 (b). Both insets in Fig. 5 (b) and (c) show the plots of real-part impedance (Z²) with respect to ω^{-1/2}. From the slop of these plots, Li⁺ diffusion coefficient for the two composites (A) and (B) was calculated, as shown in Table 2.

Table 2 Charge-transfer resistance (R_{ct}), Warburg-impedance coefficient (σ), and the Li⁺ diffusion coefficient (D_{Li}) for (A) LiMn_{0.8}Fe_{0.2}PO₄/SGCNT and (B) LiMn_{0.792}Fe_{0.198}Mg_{0.010}PO₄ /SGCNT composites. The value of R_{ct} was obtained by fitting the EIS spectra of blocking cells (Fig. 5a) with the equivalent circuit (see the inset of Fig. 5a). The value of σ the Warburg-impedance coefficient of the material, which was derived from the slopes of the plots in the insets of Fig. 5b and Fig. 5c. D_{Li} was calculated from the following equation; $D_{Li+} = 0.5$ $R^2 T^2 / S^2 n^4 F^4 C^2 \sigma^2$, where R is the gas contant, T is temperature, S is the surface area of the electrode (5 cm²), n is the number of electrons per molecule during oxidization, F is the Faraday constant, C is the concentration of the Li⁺, which was calculated using the following equation: C = 1 / nV, calculated n is Avogadro's number and V is the volume of the refined crystal lattice, taken from Table 1.

| Sample | | $R_{ct}(\Omega)$ $\sigma(\Omega \operatorname{rad}^{1/2} \operatorname{s}^{1/2})$ | | D_{Li} at 3.5 V (cm ² s ⁻¹) | D_{Li} at 4.1 V (cm ² s ⁻¹) | |
|--------|---|---|------|--|--|--|
| Α | LiMn _{0.8} Fe _{0.2} PO ₄ | 19.58 | 20.8 | 2.26 × 10 ⁻¹³ | 3.20 × 10 ⁻¹⁵ | |
| В | $LiMn_{0.792}Fe_{0.198}Mg_{0.010}PO_{4}$ | 10.22 | 10.9 | 4.96×10^{-13} | 1.16×10^{-14} | |

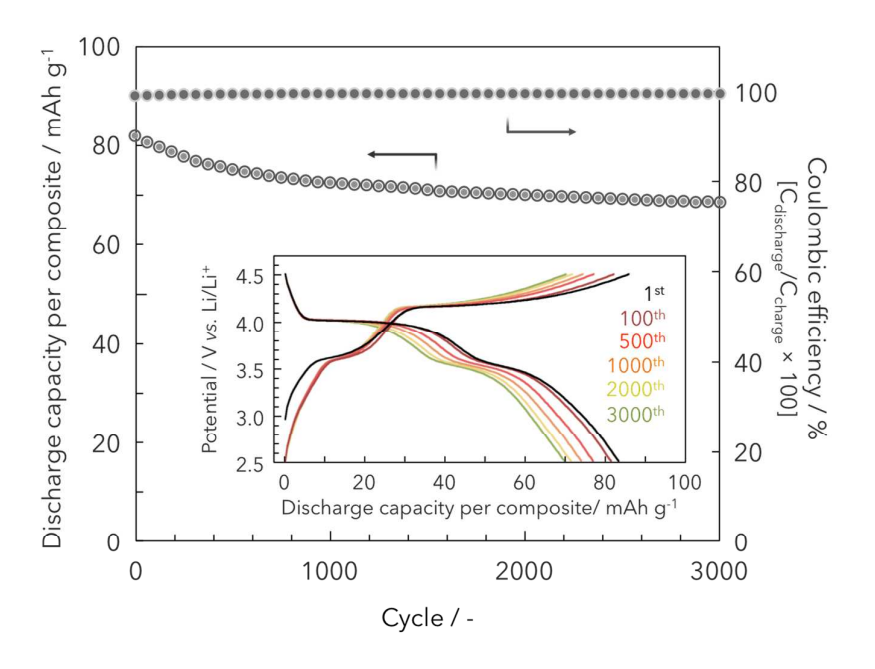


Fig. 6 Cycle-life testing for the $LiMn_{0.792}Fe_{0.198}Mg_{0.010}PO_4/SGCNT$ composite, showing stable performance over 3,000 cycles. The left ordinate corresponds to the discharge capacity per composite and the right one corresponds to the coulombic efficiency which is the percentages of the discharged capacity ($C_{discharge}$) to the C_{charge} . All experiments were set to 1 C with cycling performed under CC-mode (without CV time unlike other measurements). The inset shows the charge-discharge profiles for the $LiMn_{0.792}Fe_{0.198}Mg_{0.010}PO_4/SGCNT$ at 1st, 100th, 500th, 1,000th, 2,000th, and 3,000th cycle.